

Non-centered inversion symmetry in momentum space

Bin-Bin Liu,^{1,*} Xian-Lei Sheng,^{1,2,†} Y. X. Zhao,^{3,4,‡} and Shengyuan A. Yang^{5,6}

¹*School of Physics, Beihang University, Beijing 100191, China*

²*Peng Huanwu Collaborative Center for Research and Education, Beihang University, Beijing 100191, China*

³*National Laboratory of Solid State Microstructures and Department of Physics, Nanjing University, Nanjing 210093, China*

⁴*Collaborative Innovation Center of Advanced Microstructures, Nanjing University, Nanjing 210093, China*

⁵*Research Laboratory for Quantum Materials, Singapore University of Technology and Design, Singapore 487372, Singapore*

⁶*Center for Quantum Transport and Thermal Energy Science,
School of Physics and Technology, Nanjing Normal University, Nanjing 210023, China*

Symmetry is prevalent in physics, where the spacial inversion symmetry is one of the most important symmetries which defines the parity. It inverts the real space position as well as the momentum of a physical system relative to the original point in the real and momentum spaces. Here, we discover a new kind of inversion symmetry which inverts the real space position relative to the origin but is non-centered in the momentum space. We derive the momentum-non-centered inversion symmetry with projectively enriched symmetry algebras and demonstrate it in Hamiltonians in π flux lattices in both 2D and 3D. Intriguingly, we discover Mobius insulators with shifted-inverse edge states at half-fillings and a high Chern number insulator that has off-centered chiral edge states at quarter-fillings, which have not been reported before. We also define quantized topological numbers that indicate the existence of the novel edge states with off-centered crossing points in the momentum space. We design topological circuits that correspond to our Hamiltonian and perform simulations, which agree with our theoretical predictions. Our findings suggest new routes for exploring topological edge responses with projective symmetries in artificial systems.

Symmetry is paramount in physics. The inversion symmetry plays a vital role in determining the parity of a system and classification of topological states. While the inversion symmetry is well understood, its projective representation and how it modifies the momentum space actions, however, are barely explored. Here, we propose novel momentum nonsymmorphic inversion symmetries that have additional translations of *half* reciprocal lattice translations in the momentum space and explore its unique physical consequences in lattice models and artificial systems.

Due to a half glide of reciprocal lattice vector in the momentum space, the inversion center are shifted by a *quarter* of reciprocal lattice vector. We call it momentum-non-centered inversion symmetry (MNCIS). We propose and investigate both 2D and 3D MNCIS with inversion centers at $(n\pi, \pm\pi/2)$ [or $(\pm\pi/2, n\pi)$], $(\pm\pi/2, \pm\pi/2)$, and $(\pm\pi/2, \pm\pi/2, \pm\pi/2)$ ($n, n' = 0, \pm 1$), which are distinct from the conventional inversion centers at time-reversal invariant (TRIM) points.

Gauge field is proved of great importance to topological states of matter[1–4]. Among all the flux's values, π -flux preserves time-reversal symmetry and is valued in \mathbb{Z}_2 , which has potential to modify the symmetry algebras by switching the commutation into anti-commutation relation and vice versa[5–7]. We construct lattice models with \mathbb{Z}_2 gauge fields to realize the MNCIS.

There are two special aspects about the MNCIS. One is that the real and momentum inversion centers

are not coincides; the other is that the momentum inversion centers and the TRIM points are not coincides. Exploring the first aspect, we find that the MNCIS is essential in determining the behavior of the edge/surface states. Distinct from the edge states related by normal inversion symmetry, those related by the MNCIS have non-centered fixed points in a reduced Brillouin subspace. With this observation, we discover Mobius insulators with shifted-inverse edge states at half-fillings and a Chern insulator with a high Chern number $c_n = 2$ that has off-centered chiral edge states at quarter-fillings, which have not been reported before. The second aspect, the mismatch between TRIM points and inversion centers, lead to dramatic topological consequences. The key is that the time-reversal symmetry determines which pair of inversion centers are equivalent and band inversions are the same at equivalent centers. As a consequence, in 2D, for example, systems with inversion centers at $(\pm\pi/2, \pm\pi/2)$ has topological edge states along both edge directions, while systems with $(n\pi, \pm\pi/2)$ has only topological edge states along y-edge. In 3D, systems with inversion centers at $(\pm\pi/2, \pm\pi/2, \pm\pi/2)$ can feature 2D BZ slices of nontrivial Chern numbers, which can be used to determine the existence of Weyl points.

We define quantized topological indicators of \mathbb{Z}_2 classification to characterize the novel edge spectra and provide formulas to calculate it. It is originated from a guaranteed Berry phase $\theta = \pi$ obtained by integrating Berry connections along an 1D-subspace in the BZ across two adjacent non-centered inversion centers, which can either be read from Wilson loop spectra or from parity of the two centers.

We provide a general way of designing topological circuits to realize our lattice models and give simulation

* bblu@buaa.edu.cn

† xlsheng@buaa.edu.cn

‡ zhaoyx@nju.edu.cn

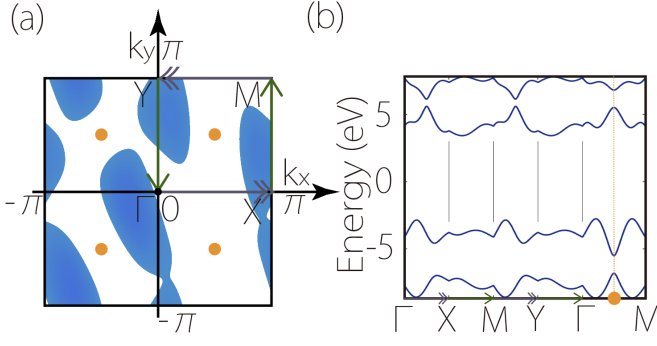


FIG. 1. (a) Energy spectra of the H_{xy}^{2D} in the first BZ with a constant energy cut-off. Centers of the MNCIS are noted as orange dots. Arrows with same colors (or shapes) are equivalent. (b) The energy spectra along high-symmetry lines in the first BZ.

results that are in good agreement with the theoretical predictions. Our setup provide a guidance for further experimental realizations in circuits. The model and theory can also be readily realized and tested in other artificial systems where adding the \mathbb{Z}_2 gauge fields preserving time-reversal symmetry are possible.

Momentum-non-centered inversion symmetry (MNCIS).— Contrary to the conventional inversion symmetry, the momentum-non-centered inversion symmetry we propose is non-symmorphic and has additional translation of half reciprocal lattice vectors, $\mathcal{P}\mathcal{L}_{G/2}$, where the G stands for reciprocal lattice vector. The P is a normal inversion symmetry with the form

$$P = U\hat{I} \quad (1)$$

where the U acts on the real space's orbital/pseudo-spin and \hat{I} on the momentum. The Hamiltonian H that possesses the P , i.e $PH P^\dagger = H$ leads to

$$UH(-\mathbf{k})U^\dagger = H(\mathbf{k}). \quad (2)$$

To realize the momentum glide, we introduce the following algebra $\{P, L_i\} = 0$. It follows that

$$PL_i P^\dagger = -L_i^{-1} = e^{i(k_i + G_i/2)a_i} \quad (3)$$

with a_i lattice vectors and $i=x,y,z$. This implies that the inversion is projectively enriched by glide of half reciprocal lattice $G_i/2$ along k_i , which yields the MNCIS:

$$\mathcal{P}_i = P\mathcal{L}_{G_i/2} \quad (4)$$

To see the how the \mathcal{P} becomes non-centered, we investigate a 2D Hamiltonian H_y^{2D} obeying the \mathcal{P}_y as an example and get

$$U_{2D}H_y^{2D}(-k_x, -k_y + \pi)U_{2D}^\dagger = H_y^{2D}(k_x, k_y). \quad (5)$$

As a result, the inversion centers of the \mathcal{P}_y^{2D} are shifted a *quarter* of reciprocal lattice vector G_y along k_y and

becomes $(n\pi, \pm\pi/2)$ ($n = 0, \pm 1$). Note that the real space inversion centers stay still— $(na/2, n'b/2)$ — which are centered in the unite cell.

The momentum glides can be added freely in different directions. Apart from $\{P, L_y\} = 0$, if we further implement $\{P, L_x\} = 0$, it leads to

$$\mathcal{P}_{xy}^{2D} = U^{2D}\mathcal{L}_{G_x/2}\mathcal{L}_{G_y/2}\hat{I}_{xy} \quad (6)$$

A Hamiltonian that obeys Eq. (6) gives rise to

$$UH_{xy}^{2D}(-k_x + \pi, -k_y + \pi)U^\dagger = H_{xy}^{2D}(k_x, k_y). \quad (7)$$

The \mathcal{P}_{xy} has inversion centers at $(\pm\pi/2, \pm\pi/2)$. It can even be extended in 3D as

$$\mathcal{P}_{xyz}^{3D} = U_{3D}\mathcal{L}_{G_x/2}\mathcal{L}_{G_y/2}\mathcal{L}_{G_z/2}\hat{I}_{xyz} \quad (8)$$

which characterizes

$$U_{3D}H_{xyz}^{3D}(-k_x + \pi, -k_y + \pi, -k_z + \pi)U_{3D}^\dagger = H_{xyz}^{3D}(k_x, k_y, k_z). \quad (9)$$

Next, we demonstrate these MNCISs in physical systems and reveal their physical consequences.

Physical Realizations of MNCISs in 2D and 3D models.— The key to realizing the MNCIS \mathcal{P} is to have projective symmetry algebras. In tight-binding conventions, the additional π -phase required by the anti-symmetric symmetry algebras can be achieved through negative topplings. We apply the \mathbb{Z}_2 gauge fields on π -flux lattices to construct our models.

To realize a Hamiltonian with \mathcal{P}_{xy}^{2D} , we construct a lattice model as shown in Fig. 2 (a). All red bonds are attached with a π phase and hence are minus, as $e^{i\pi} = -1$. The bond width indicates the magnitude. In the unite cell convention, the inversion operation flips the gauge configuration (i.e., the position of the red bonds), but preserves the dimerization pattern and the flux configuration. The anti-commutation $\{P, L_i\} = 0$ comes from a π phase acquired by the L_i following a closed path by $PL_iP^{-1}L_i^{-1}$, which is evidenced from the Fig. 2 (a). We break the time-reversal symmetry, which is centered at TRIM points, to demonstrate the our model construction. The spectra of the model is show in Fig. 1 (a), where the inversion centers are in each quadrants of the BZ. Following the prescription, we can also construct a model for the \mathcal{P}_y^{2D} as shown in Fig. 3 (a). The resulting Hamiltonian H_y^{2D} possesses the momentum non-centered inversions as shown in Fig. 3 (a).

One prominent consequence of the MNCIS lies in its modification on the edge spectra. For a 2D slab geometry with periodic i (k_i), the MNCIS is projected as

$$\mathcal{P}_i^{slab} = U_{2D}^{slab}\mathcal{L}_{G_i/2}\hat{I}_i \quad (10)$$

where the U_{2D}^{slab} is the real space inversion operation of the orbitals of the slab. This means that the two edges of the slab related by U_{slab} may characterize states that are related by a non-centered inversion in k_y subspace,

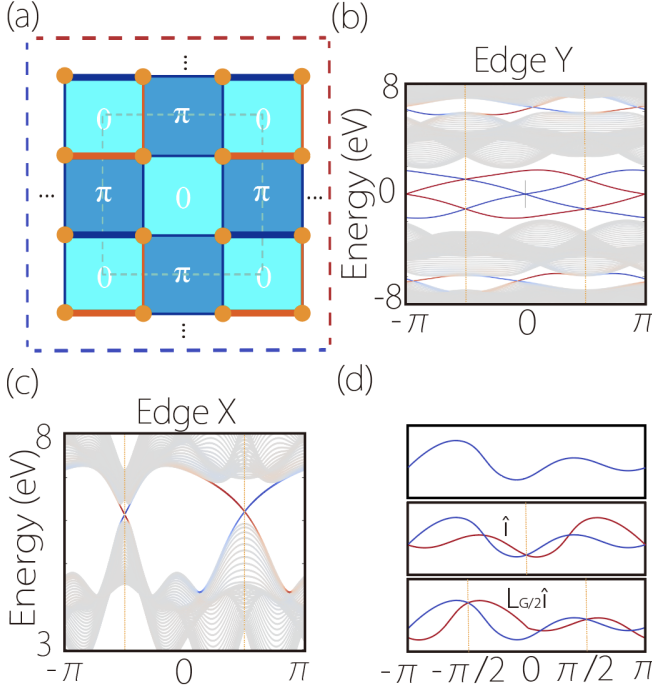


FIG. 2. Lattice model and spectra with the \mathcal{P}_{xy}^{2D} symmetry. (a) 2D lattice model with gauge distributions and dimerization patterns specified. Each red bond is attached with a π flux as $e^{i\pi} = -1$. The flux through each plaquette is determined by the number of red bond forming it. The bond width indicates the magnitude of the bond. The unit cell is outlined with gray dashed square. (b) and (c) are edge states along Y and X edges specified in (a), with colors (red and blue) indicating the location of the edges. The edge states preserve Eq. (11). The model features Mobius insulators with shifted-inverse edge states at half-fillings and a Chern insulator with a high Chern number $c_n = 2$ that has off-centered chiral edge states at quarter-fillings, which have not been reported before. (d) Schematic plot for the edge states related by non-centered inversion symmetry in a 1D slab and the comparison with the centered chiral edge states, where \hat{I} and $\mathcal{L}_{G/2}$ are momentum space inversion and translation of half reciprocal lattice vector.

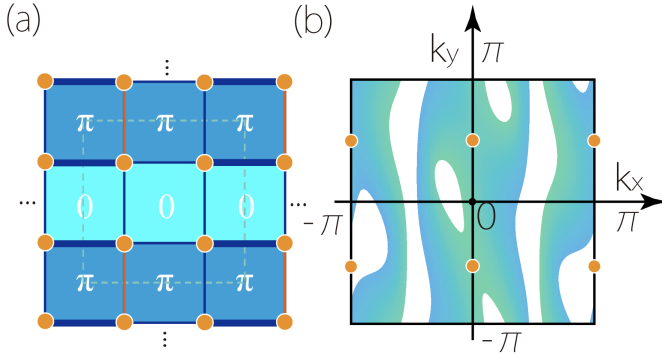


FIG. 3. Lattice model and spectra with the \mathcal{P}_y^{2D} symmetry. (a) The lattice model. (b) The band structure in the first BZ with an energy cut-off. The dots are inversion centers which line both in and on the boundary of the BZ.

distinct from the edge states related by normal inversion symmetry, as shown in the Fig. 2 (d), where the dashed lines show a shift in 1D inversion/reflection centers.

This observation explains the edge spectra in Fig. 2 (b) (c), where the blue and red lines are the states localized at opposite edges [Fig. 3 (a)]. The combination of the states from two edges has fixed points at $\pm\pi/2$ in the reduced BZ. Intriguingly, our model for the H_{xy}^{2D} features Mobius insulators with shifted-inverse edge states at half-fillings and a Chern insulator with a high Chern number, $c_n = 2$, that has off-centered chiral edge states at quarter-fillings, which have not been reported before.

The topological edge states here are stable, since addition of trivial atomic bands does not affect the nontrivial topological edge states, which can be described in K-theoretical approach.

This construction methodology can be extended to 3D. In order to have inversion symmetry that is off-center in three axial directions, \mathcal{P}_{xyz}^{3D} , additional \mathbb{Z}_2 gauge fields are needed in the third axis. We demonstrate this idea in a 3D lattice model in Fig. 4. It has eight orbits per unit cell, and every slice of it features a strip pattern of π flux. The model obeys Eq. (9) and has MNCIS defined in the Eq. (8). As a consequence, the surface states formed by two opposite surface has non-centered fixed points, as shown in Fig. 4 (d), which is a generalization of Fig. 2 (d).

$$\mathcal{P}_{ij}^{slab} = U_{3D}^{slab} \mathcal{L}_{G_i/2} \mathcal{L}_{G_j/2} \hat{I}_{ij} \quad (11)$$

where the U_{3D}^{slab} is the real space inversion operation of the orbitals of the slab. With similar way, one can extend to construct the model with MNCIS to any higher dimensions.

Fig. 4 (c) shows one possible configuration of inversion eigenvalue (+/-) for a particular band. The Chern number on the three grey planes are all nontrivial and equals to one due to the mismatch between the inversion plane and the TRIM. Since the plane that across the TRIM points must have trivial Chern numbers, this nontrivial Chern planes indicates the existence of Weyl semimetal.

To realize other 3D MNCISs one may Stack the 2D models for H_{xy}^{2D} (or H_y^{2D}) with no z flux and respecting the inversion symmetry. See Fig. 5 (e) in the SM.

Topological indicators for shifted-inverse edge states.— To characterize the topology, we investigate a well-defined vector space over a loop bundle on the Brillouin manifold around an inversion center. We formulate expression for a topological indicator defined on a quarter of BZ an inversion center.

A square BZ can be divided into four parts with respect of the four inversion centers. Each quadrant is dubbed as τ_i with $i = a, b, c, d$. See Fig. 5 (a) (b). With such segmentation, each quarter can give rise to a quantized topological number. Applying the Stokes' theorem, we have $\int_{\tau_i} \mathcal{F}(\mathbf{k}) d^2\mathbf{k} - \int_{\partial\tau_i} \mathcal{A}(\mathbf{k}) d\mathbf{k} = 0$, with $\mathcal{F}(\mathbf{k})$ and $\mathcal{A}(\mathbf{k})$ the Berry curvature and Berry phase

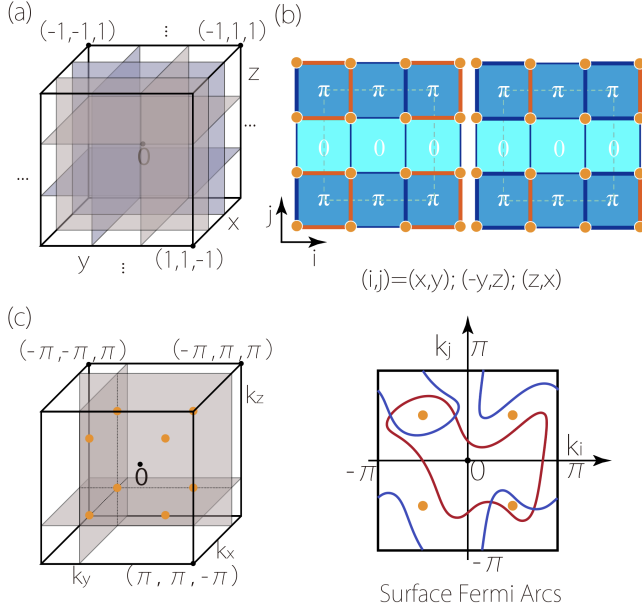


FIG. 4. 3D model with the \mathcal{P}_{xyz}^{3D} symmetry. (a) The 3D model in the real space is made of two kinds of 2D slices. Each of the dark blue slices is made of the 2D lattice in the left part of the (b); each of the lighter slices is represented by the 2D lattice in the right part of the (b). The 3D model has 8 sites per unite cell and is extended in three spacial dimensions. (c) The illustration of MNCIS with inversion center at $(\pm\pi/2, \pm\pi/2, \pm\pi/2)$ corresponding to the model in (a). The red dots are the centers with \pm sign showing one possible configuration of inversion eigenvalue for a particular band. The Chern number on the three grey planes are all nontrivial and equals to one due to the mismatch between the inversion plane and the TRIM. (d) illustrates the surface Fermi arcs of a 3D model with the MNCIS, which have reduced MNCIS and can be viewed as extension of Fig. 2 (d).

defined for isolated and continuous bands. Here both the systems have four isolated bands, where the first and third (second and forth) bands defines sub-spaces. The following topological invariants are defined for the sub-vector spaces, i.e., $V(\mathbf{k}) = \text{span}[\psi_n(\mathbf{k})]$ ($n = 1$ or 2).

Take H_{xy}^{2D} as an example. The boundary of each τ_i is composed of four parts: right (R), up (U), left (L), down (D). Due to the equivalence of diagonal points, e.g., $(0,0)$ and (π,π) or $(0,-\pi/2)$ and $(\pi,\pi/2)$, the D+R forms a closed loop on which the loop boundle defines a berry phase $\gamma(D+R)$. Restricted by the non-orientable edge connections, the $\gamma(U+L)$ is nothing but $\gamma(D+R)$. Therefore, we define a topological indicator for each τ_i as

$$u_i = \frac{1}{2\pi} \int_{\tau_i} \mathcal{F}(\mathbf{k}) d^2\mathbf{k} - \frac{1}{\pi} \gamma(D+R) \mod 2. \quad (12)$$

In the nontrivial case with $(\pm\pi/2, \pm\pi/2)$, we obtain $u_a = u_d = 0$ and $u_b = u_c = 1$. In the nontrivial case with $(n\pi, \pm\pi/2)$, we find $u_a = u_c = 0$ and $u_b = 1, u_d = 1$. See Fig. 5 (a) (b). In the trivial cases, all $u_i = 0$.

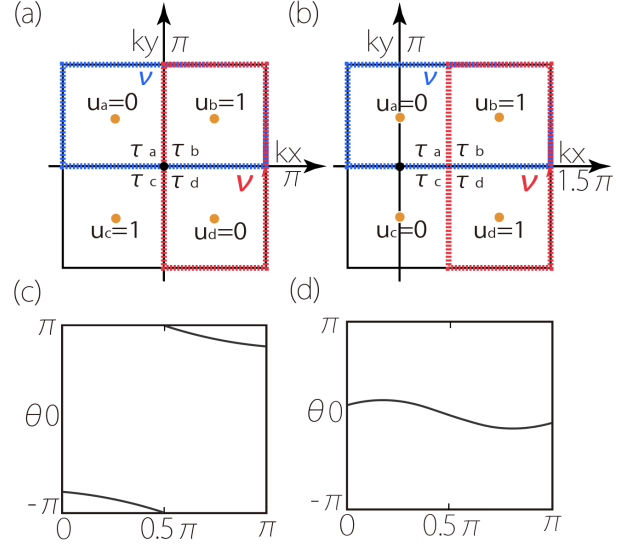


FIG. 5. Topological indicators u_i and the Wilson loop. The distribution of u_i for (a) the H_{xy}^{2D} and (b) the H_y^{2D} . The ν (ν') defined on the union of two adjacent quadrants is a \mathcal{Z} invariant, which can be read from the Wilson loop—(c) for nontrivial and (d) for trivial ν (ν'). In the nontrivial case, it is guaranteed that a Berry phase $\theta = \pi$ occurs when integrated on a line across two non-centered inversion centers.

To give a geometric apprehension, we take the union of two adjacent quadrants, e.g., $\tau_a \cup \tau_b$ on which the Wilson loop can be calculated. Adding u_a and u_b , we can define

$$\begin{aligned} \nu &= u_a + u_b \mod 2 \\ &= \frac{1}{2\pi} \int_{\tau_a \cup \tau_b} \mathcal{F}(\mathbf{k}) d^2\mathbf{k} - \frac{1}{\pi} \gamma(k_y = 0) \mod 2 \end{aligned} \quad (13)$$

Similarly, we can define

$$\begin{aligned} \nu' &= u_b + u_d \mod 2 \\ &= \frac{1}{2\pi} \int_{\tau_b \cup \tau_d} \mathcal{F}(\mathbf{k}) d^2\mathbf{k} + \frac{1}{\pi} \gamma(k_x = 0) \mod 2 \end{aligned} \quad (14)$$

We emphasise that the second terms of ν and ν' are different in a sign. The above Eq. (13) and Eq. (14) can be read off from Wilson loop. Take ν' as an example. Since $\int_{\tau_b \cup \tau_d} \mathcal{F}(\mathbf{k}) d^2\mathbf{k} = \gamma(k_x = \pi) - \gamma(k_x = 0)$, we then have

$$\begin{aligned} \nu'(\nu) &= \frac{1}{2\pi} [\gamma(0) + \gamma(\pi)] \mod 2 \\ &= \zeta \mod 2 \end{aligned} \quad (15)$$

where the ζ is a geometric quantity that counts the times of crossings of the Wilson loop spectrum with the $\theta = \pi$ line. Therefore, we can infer the information of edge states from the u_i , such as the existence of edge states along certain edges.

We can further formulate the u_i to relate the parity

eigenvalue λ_i at the inversion center Γ_j ,

$$(-1)^{u_a+u_b} = (-1)^\nu = \prod_{j=a,b} \prod_i^N \lambda_i(\Gamma_j) \quad (16)$$

and similarly,

$$(-1)^{u_b+u_d} = (-1)^{\nu'} = \prod_{j=b,d} \prod_i^N \lambda_i(\Gamma_j) \quad (17)$$

The Γ_j are the inversion centers in the τ_j quadrants of the BZ. Different from the previous \mathbb{Z}_2 number, the Γ_j do not coincide with the time-reversal invariant momenta, but are nonsymorphic, such that $\Gamma_j = (\pm\pi/2, \pm\pi/2)$. In our examples, the occupation number of the sub system is $N = 1$. The detailed derivations are presented in the SM C. The off-centered parity eigenvalues of our models are in SMB.

Different inversion centers relative to the TRIM points lead to different topological consequences. For the $(n\pi, \pm\pi/2)$ case, it admits topological classification by ν in Eq. (13), which features edge state only along y. The situation is different for the $(\pm\pi/2, \pm\pi/2)$ case, as it features another topological invariant ν' in the nontrivial case. Therefore, not only the y edges [Fig. 2 (b)] but also the x edges [Fig. 2 (c)] host topological states.

The edge states we discussed here are stable topological, which are robust against adding trivial bands, as they are described within the K-theory.

Experimental realizations of MNCIS—Enjoying the development of artificial systems, the MNCIS can find experimental realizations and applications in cold atoms, optical lattices, circuits, phonons and meta-materials. Based on our TB models, we demonstrate this idea in topological circuits. We find very components of the TB models their circuits correspondences, see Fig. 10 in the SM, and hence map the Hamiltonian into a circuits' Laplacian obtained by Kirchhoff's node-current law[8].

In topological circuit, the square-root of the positive energy is mapped to the frequency of circuit, $\omega \sim \sqrt{E_{shifted}}$, where the $E_{shifted}$ are the eigenvalues shifted all to positive. As an example, we simulate the H_{xy}^{2D} in the Fig. 2 (a) in a circuit device of 21×21 unites with periodic and open boundary conditions in two directions.

The simulation results are shown in Fig. 6, which shows the non-centered chirality of the edges states. Notably, the simulation results (light dots) are in perfect agreement with theoretical predictions (thin dashed lines), which demonstrates the validity of our circuit setups and paves the way for experiments.

Conclusion and discussion— In conclusion, with modified symmetry algebras, we discover a new kind of inversion symmetry which inverses the real space position relative to the origin but is non-centered in the momentum space. We derive this non-centered momentum with projectively enriched symmetry algebras. We demonstrate the idea in Hamiltonians on

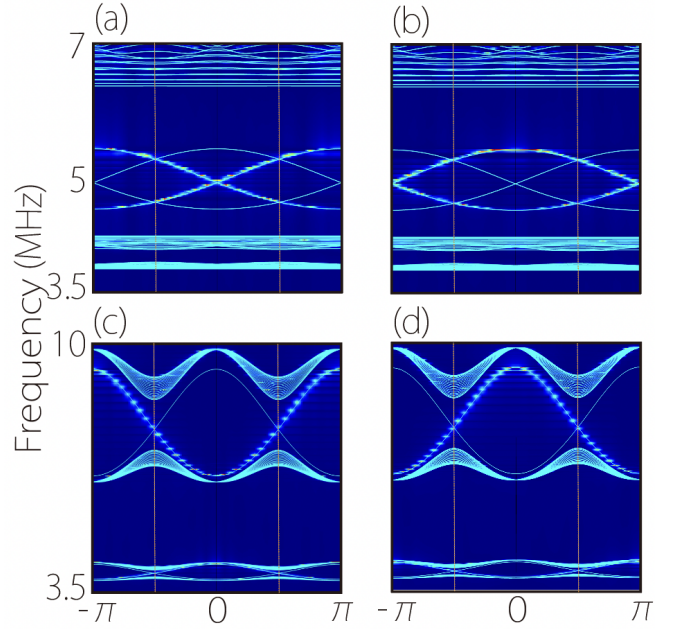


FIG. 6. Circuits' simulation results for the lattice TB model with the \mathcal{P}_{xy}^{2D} symmetry in the Fig.2. The bright yellow dots are the simulation results which are in agreement with the theoretical predictions (cyan lines). The edge states for the left (a), right (b), bottom (c) and top (d) edges are presented, which satisfy the non-centered inversion symmetry for slab geometries with the convention in the Fig.2 (a). The spectra are rescaled with relations in Eq. (E6).

flux lattices with \mathbb{Z}_2 gauge field, which naturally realize the non-centered momentum inversion symmetries. We also discover unconventional \mathbb{Z}_2 topological indicators emergent from the gauge fields, which are protected by the momentum-non-centered symmetries. The topological numbers ν and ν' can be read off from Wilson loops evolving along both reciprocal lattice vectors. We further map We find that non-trivial topological indicators defined along both vectors signal a novel topological insulator, with both of its x and y edges (four edges) hosting edge states linked by a reduced non-centered inversion symmetry in each pairs, drastically distinct from previous topological insulators.

We propose a circuits setup for our model and provide simulation results that are in good agreement with the theories' predictions. Our setup provide a guidance for further experimental realizations in circuits. The model and theory can also be readily realized and tested in other artificial systems where adding the \mathbb{Z}_2 gauge fields preserving time-reversal symmetry are possible.

Our theory opens new routes for exploring physical and topological consequences associated with the momentum-non-centered inversion symmetries. We give an example on how to use the u_i to detect the oddity of Chern number. See SM E. The next theoretical pursuits would be to explore non-centered \mathcal{PT} symmetry and its topological classification, which we briefly discussed in

the SM.

ACKNOWLEDGMENTS

We thank Rui Yu and D. L. Deng for helpful discussions. We acknowledge the computational support

from HPC of the Beihang University and Texas Advanced Computing Center. This work is supported by National Key R & D Program of China (2022YFA1402600), the NSFC (Grants No. 12174018, No. 12074024), the Fundamental Research Funds for the Central Universities, and the Singapore Ministry of Education AcRF Tier 2 (T2EP50220-0026).

-
- [1] F. D. M. Haldane, *Phys. Rev. Lett.* **61**, 2015 (1988).
 - [2] C. L. Kane and E. J. Mele, *Phys. Rev. Lett.* **95**, 146802 (2005).
 - [3] B. A. Bernevig, T. L. Hughes, and S.-C. Zhang, *Science* **314**, 1757 (2006), <https://www.science.org/doi/pdf/10.1126/science.1133734>.
 - [4] X.-L. Qi, Y.-S. Wu, and S.-C. Zhang, *Phys. Rev. B* **74**, 085308 (2006).
 - [5] Y. X. Zhao, Y.-X. Huang, and S. A. Yang, *Phys. Rev. B* **102**, 161117 (2020).
 - [6] Y. X. Zhao, C. Chen, X.-L. Sheng, and S. A. Yang, *Phys. Rev. Lett.* **126**, 196402 (2021).
 - [7] Z. Y. Chen, S. A. Yang, and Y. X. Zhao, *Nature Communications* **13**, 2215 (2022).
 - [8] S. Imhof, C. Berger, F. Bayer, J. Brehm, L. W. Molenkamp, T. Kiessling, F. Schindler, C. H. Lee, M. Greiter, T. Neupert, *et al.*, *Nature Physics* **14**, 925 (2018).
 - [9] L. Fu and C. L. Kane, *Phys. Rev. B* **76**, 045302 (2007).
 - [10] R. Yu, Y. X. Zhao, and A. P. Schnyder, *National Science Review* **7**, 1288 (2020), <https://academic.oup.com/nsr/article-pdf/7/8/1288/38882379/nwaa065.pdf>.

Supplementary materials for “Non-centered inversion symmetry in momentum space”

Appendix A: Model and Methods

1. 2D models

The generic 2D TB model in square lattices with four orbitals per unite cell (Fig. 7) written in k-space has the form

$$H_0 = \begin{pmatrix} 0 & tm_1 + tm_2 e^{k_x i} & lm_1 + lm_2 e^{-k_y i} & 0 \\ tm_1 + tm_2 e^{-k_x i} & 0 & 0 & l_1 + l_2 e^{-k_y i} \\ lm_1 + lm_2 e^{k_y i} & 0 & 0 & t_1 + t_2 e^{k_x i} \\ 0 & l_1 + l_2 e^{k_y i} & t_1 + t_2 e^{-k_x i} & 0 \end{pmatrix} \quad (A1)$$

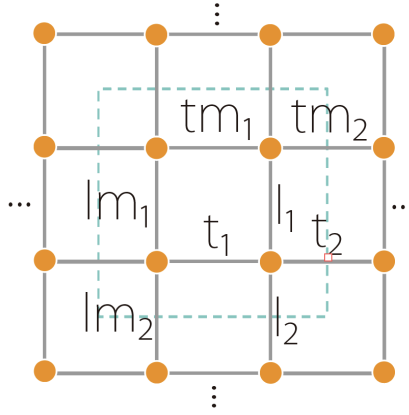


FIG. 7. The generic 2D TB model.

a. The H_y^{2D}

To get the Fig. 3 in the main text, we break the $\mathcal{T} = \mathcal{K}$ symmetry and expose the non-centered feature of \mathcal{P}_y by introducing

$$H_{y1} = \sin(k_x)\tau_x\sigma_y + \cos(k_x)\tau_y\sigma_y \quad (A2)$$

and

$$H_{y2} = \sin(k_y)\tau_y\sigma_y + \cos(k_y)\tau_x\sigma_y. \quad (A3)$$

The resulting lattice models in momentum space can be written as,

$$H_y^{2D} = H_0 + \lambda[H_{y1} + H_{y2}]. \quad (A4)$$

For the H_0 , we set the parameters as $t_1 = 1.5$, $t_2 = 5.5$, $tm_1 = 1.5$, $tm_2 = 5.5$, $lm_1 = 1.0$, $lm_2 = -1.0$, $l_1 = 1.0$, $l_2 = 1.0$, and the $\lambda = 1$ in the unite of eV.

b. The H_{xy}^{2D}

To get the Fig. 1 in the main text, we break the \mathcal{T} symmetry and expose the non-centered feature of \mathcal{P}_{xy} by introducing perturbation terms

$$H_{xy1} = \sin(k_x)\tau_y\sigma_y + \cos(k_x)\tau_y\sigma_x \quad (A5)$$

$$H_{xy2} = \sin(k_y)\tau_y\sigma_y + \cos(k_y)\tau_y\sigma_x. \quad (\text{A6})$$

The resulting Hamiltonian has no time-reversal $\mathcal{T} = \mathcal{K}$ and sub-lattice symmetry $\mathcal{S} = \tau_z\sigma_z$ which the H_0 has. The resulting lattice models in momentum space can be written as,

$$H_{xy}^{2D} = H_0 + \lambda[H_{xy1} + H_{xy2}]. \quad (\text{A7})$$

For the H_0 , we set $t_1 = 1.5$, $t_2 = 5.5$, $tm_1 = 1.5$, $tm_2 = -5.5$, $lm_1 = 1.0$, $lm_2 = -1.0$, $l_1 = 1.0$, $l_2 = 1.0$, in the unite of eV, and $\lambda = 1.5$ eV for calculating the bulk/edge and the Wilson loop spectra.

2. The 3D models

The 3D model is the stacking of two layers of 2D models H_0 (top and bottom layers) with interlayer hopping H_{inter} ,

$$H^{3D} = \begin{pmatrix} H_0^T & H_{inter} \\ H_{inter}^\dagger & H_0^B \end{pmatrix}, \quad (\text{A8})$$

$$(\text{A9})$$

With

$$H_{inter} = \begin{pmatrix} pa_1 + pa_2 e^{k_z i} & 0 & 0 & 0 \\ 0 & pb_1 + pb_2 e^{k_z i} & 0 & 0 \\ 0 & 0 & pc_1 + pc_2 e^{k_z i} & 0 \\ 0 & 0 & 0 & pd_1 + pd_2 e^{k_z i} \end{pmatrix}. \quad (\text{A10})$$

a. Parameters for the model for H_{xyz}^{3D}

For the H_{xyz}^{3D} in the Fig. 4 in the main text, the parameters for the interlayer H_{inter} are set as $pa_1 = pd_1 = 1$, $pa_2 = -5$, $pd_2 = 5$, $pb_1 = pc_1 = 5$, $pb_2 = -1$, $pc_2 = 1$, in the unite of eV. For the H_0^T , the parameters are $t_1 = 1$, $t_2 = -5$, $tm_1 = 1$, $tm_2 = -10$, $lm_1 = 1$, $lm_2 = -5$, $l_1 = 1$, $l_2 = 10$, in the unite of eV; for H_0^B , the parameters are $t_1 = 1$, $t_2 = 5$, $tm_1 = 1$, $tm_2 = 10$, $lm_1 = 1$, $lm_2 = -5$, $l_1 = 1$, $l_2 = 10$, in the unite of eV.

b. The model for H_{xy}^{3D}

Stacking the model of H_{xy}^{2D} , with respect of the inversion symmetry, we extend the H_{xy}^{2D} to a higher dimension. See Fig. 8 (e). There are eight orbitals per unite cell.

In 3D, the non-centered inversion of the system becomes

$$\mathcal{P}_{xy}^{3D} = U_{3D} \mathcal{L}_{G_x/2} \mathcal{L}_{G_y/2} \hat{I} \quad (\text{A11})$$

Each of the Hamiltonian's momentum k_z -plane obeys non-centered $(\pm\pi/2, \pm\pi/2)$ symmetry

$$U_{3D} H_{xy}^{3D}(-k_x + \pi, -k_y + \pi, -k_z) U_{3D}^\dagger = H_{xy}^{3D}(k_x, k_y, k_z). \quad (\text{A12})$$

By properly dimerize the interlayer hopping, we create a topological surface state with inversion at $(\pm\pi/2, \pm\pi/2)$. See Fig. 8 (a) and (b). The topology can be identified by the band inversion at half-fillings between $k_z = 0$ and $k_z = \pi$ planes. Since the model has four non-centered inversion centers on each k_z plane, we calculate the parity eigenvalues of the H_{3D} at the centers, which indeed indicates a single band inversion between the two planes. See Tab. V.

For the nontrivial case, the parameters are set as $pa_1 = pd_1 = 1$, $pa_2 = pd_2 = 10$, $pb_1 = pc_1 = 2$, $pb_2 = pc_2 = 1$, in the unite of eV. For the H_0^T or H_0^B , we set $t_1 = 1.5$, $t_2 = 5.5$, $tm_1 = 1.5$, $tm_2 = -5.5$, $lm_1 = 1.0$, $lm_2 = -1.0$, $l_1 = 1.0$, $l_2 = 1.0$, in the unite of eV.

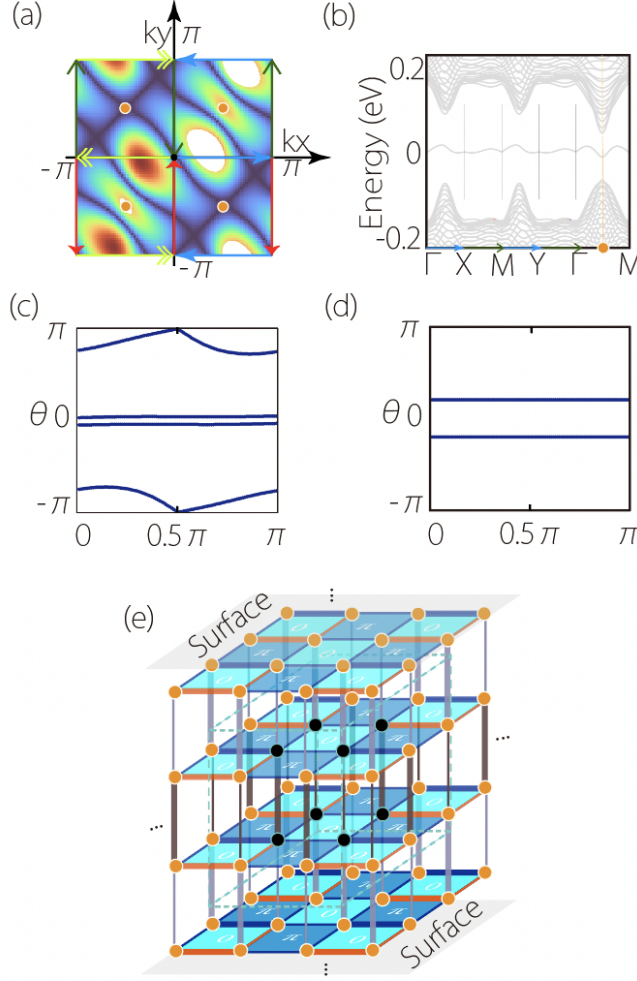


FIG. 8. 3D topological insulator with $(\pm\pi/2, \pm\pi/2)$ surface state. (a) The surface state around Fermi level with a constant cut off at 0.1 eV to show the non-centered inversion. (b) The surface and projected bulk states along a line denoted in (a) specified by the arrows. The colors indicates the dispersions in energy. The orange dots are defined in (a) with the orange line showing the reflection symmetry. The Wilson loop calculated in τ_1 domain at (c) $k_z = 0$ and (d) $k_z = \pi$, which are nontrivial and trivial. (e) The lattice model for the surface state in (a), with the dashed lines on a cubic enclosing the eight sites marked as black dots in a unite cell.

Appendix B: Parity eigenvalues of the models

We now calculate the parity eigenvalues for our models under different gauge fields. The parity eigenvalues for the 2D models H_y^{2D} and H_{xy}^{2D} are listed in the TABLE I and II, which shows different configurations and hence features distinct topological properties. The key to understand this lies in the mismatch between TRIM point and inversion centers. The time-reversal symmetry determines which pair with inversion centers are equivalent. Therefore, band inversion at these centers are the same. In the H_y^{2D} , the inversion centers in a column (with the same k_y) are equivalent, while the diagonal centers are equivalent for the H_{xy}^{2D} . This leads to a dramatic topological consequence that, both edges of the H_{xy}^{2D} host nontrivial edge states while the H_y^{2D} can only have topological y-edge, which are evidenced from a π Berry phase integrated long the 1D-subspace.

To understand the edge states at both half and quarter fillings of H_{xy}^{2D} along different edge directions, we provide a illustration of atomic band inversions in TABLE III. The atomic bands, a, b, c, d, have parity eigenvalues 1, -1, -1, 1. The a and c (b and d) bands are inverted in the transverse direction, while the a and b (c and d) bands the longitudinal direction, which indicates edge states at half and quarter fillings in the main text. This is in agreement with the nontrivial ν and ν' calculated in the main text.

Similarly we present the parity eigenvalues of the 3D models, H_{xy}^{3D} and H_{xyz}^{3D} in the main text, listed in the TABLE IV and V.

TABLE I. The parity eigenvalues of H_y^{2D} 's bands at inversion centers $(n\pi, \pm\pi/2)$.

| Band index i | $(0, \pi/2)$ | $(\pi, \pi/2)$ | $(0, -\pi/2)$ | $(\pi, -\pi/2)$ |
|----------------|--------------|----------------|---------------|-----------------|
| 1 | 1 | -1 | 1 | -1 |
| 2 | -1 | 1 | -1 | 1 |
| 3 | -1 | 1 | -1 | 1 |
| 4 | 1 | -1 | 1 | -1 |

TABLE II. The parity eigenvalues of H_{xy}^{2D} 's bands at inversion centers $(\pm\pi/2, \pm\pi/2)$.

| Band index i | $(-\pi/2, \pi/2)$ | $(\pi/2, \pi/2)$ | $(-\pi/2, -\pi/2)$ | $(\pi/2, -\pi/2)$ |
|----------------|-------------------|------------------|--------------------|-------------------|
| 1 | 1 | -1 | -1 | 1 |
| 2 | -1 | 1 | 1 | -1 |
| 3 | -1 | 1 | 1 | -1 |
| 4 | 1 | -1 | -1 | 1 |

TABLE III. Illustration of atomic band inversions that yields edge states at half and quarter fillings. The atomic bands are a, b, c, d, which have parity eigenvalues 1, -1, -1, 1. The a and c (b and d) bands are inverted in the transverse direction, while the a and b (c and d) bands the longitudinal direction, which indicates edge states at half and quarter fillings in the main text.

| Band index i | $(-\pi/2, \pi/2)$ | $(\pi/2, \pi/2)$ | $(-\pi/2, -\pi/2)$ | $(\pi/2, -\pi/2)$ |
|----------------|-------------------|------------------|--------------------|-------------------|
| 1 | a | c | b | d |
| 2 | b | d | a | c |
| 3 | c | a | d | b |
| 4 | d | b | c | a |

TABLE IV. The parity eigenvalues of H_{xyz}^{3D} ' bands at inversion centers $(\pm\pi/2, \pm\pi/2, n\pi)$.

| Band index i | $k_z = 0$ | | | | $k_z = \pi$ | | | |
|-------------------|-------------------|------------------|--------------------|-------------------|-------------------|------------------|--------------------|-------------------|
| | $(-\pi/2, \pi/2)$ | $(\pi/2, \pi/2)$ | $(-\pi/2, -\pi/2)$ | $(\pi/2, -\pi/2)$ | $(-\pi/2, \pi/2)$ | $(\pi/2, \pi/2)$ | $(-\pi/2, -\pi/2)$ | $(\pi/2, -\pi/2)$ |
| 1 | -1 | 1 | 1 | -1 | 1 | -1 | -1 | 1 |
| 2 | 1 | -1 | -1 | 1 | -1 | 1 | 1 | -1 |
| 3 | 1 | -1 | -1 | 1 | -1 | 1 | 1 | -1 |
| 4 | 1 | -1 | -1 | 1 | 1 | -1 | -1 | 1 |
| 5 | -1 | 1 | 1 | -1 | -1 | 1 | 1 | -1 |
| 6 | -1 | 1 | 1 | -1 | 1 | -1 | -1 | 1 |
| 7 | -1 | 1 | 1 | -1 | 1 | -1 | -1 | 1 |
| 8 | 1 | -1 | -1 | 1 | -1 | 1 | 1 | -1 |

TABLE V. The parity eigenvalues of H_{xyz}^{3D} ' bands at inversion centers $(\pm\pi/2, \pm\pi/2, \pm\pi/2)$.

| Band index i | $k_z = -\pi/2$ | | | | $k_z = \pi/2$ | | | |
|-------------------|-------------------|------------------|--------------------|-------------------|-------------------|------------------|--------------------|-------------------|
| | $(-\pi/2, \pi/2)$ | $(\pi/2, \pi/2)$ | $(-\pi/2, -\pi/2)$ | $(\pi/2, -\pi/2)$ | $(-\pi/2, \pi/2)$ | $(\pi/2, \pi/2)$ | $(-\pi/2, -\pi/2)$ | $(\pi/2, -\pi/2)$ |
| 1 | -1 | 1 | -1 | -1 | -1 | -1 | 1 | -1 |
| 2 | 1 | -1 | 1 | 1 | 1 | 1 | -1 | 1 |
| 3 | 1 | -1 | 1 | 1 | 1 | 1 | -1 | 1 |
| 4 | -1 | 1 | -1 | -1 | -1 | -1 | 1 | -1 |
| 5 | 1 | -1 | 1 | 1 | 1 | 1 | -1 | 1 |
| 6 | -1 | 1 | -1 | -1 | -1 | -1 | 1 | -1 |
| 7 | -1 | 1 | -1 | -1 | -1 | -1 | 1 | -1 |
| 8 | 1 | -1 | 1 | 1 | 1 | 1 | -1 | 1 |

Appendix C: Expressing the u_i with the parity eigenvalue

In the main text, the topological number u_i are related with ν or ν' through Eq. (13) and Eq. (14), to yield a intuitive geometric pumping interpretation. Based on the discussion, we consider a 1D system k_1 , on which we can define a Berry phase (or the so-called polarization) $\gamma(k_2)$ for a fixed k_2 . Following the Ref. [9], we may define a polarization as

$$P = \int \mathcal{A}(k_1) dk_1 \quad (C1)$$

where the $\mathcal{A}(k) = \langle j, k | \nabla_k | j, k \rangle$ is the Berry potential over the 1D k -system, and $|j, k\rangle$ is the j th quantum state of the system at k .

Under the non-centered inversion symmetry in Eq. (6), the quantum state $|k\rangle$ is mapped to $|-k + \pi\rangle$. So we define a sewing matrix that relates the two states as

$$B_{ij}(k) = \langle i, -k + \pi | U | j, k \rangle \quad (C2)$$

where U is the inversion operator \mathcal{P} without momentum operations. We then have,

$$B_{ij}^*(k) U | j, k \rangle = | i, -k + \pi \rangle \quad (C3)$$

The $\mathcal{A}(k)$ can be related to $\mathcal{A}(-k + \pi)$ by the sewing matrix $B(k)$ as

$$\mathcal{A}(-k + \pi) = -\mathcal{A}(k) + i \text{Tr}[B(k) \nabla_k B^\dagger(k)]. \quad (C4)$$

The second term above can be simplified as

$$i \text{Tr}[B(k) \nabla_k B^\dagger(k)] = -i \nabla_k \log \det B(k). \quad (C5)$$

The polarization can be transformed as

$$P = \int \mathcal{A}(k) dk \quad (C6)$$

$$= \int_{-\pi/2}^{\pi/2} \mathcal{A}(k) dk + \int_{\pi/2}^{3\pi/2} \mathcal{A}(k) dk \quad (C7)$$

$$= \int_{-\pi/2}^{\pi/2} \mathcal{A}(k) dk + \int_{-\pi/2}^{\pi/2} \mathcal{A}(-k + \pi) dk \quad (C8)$$

$$= \int_{-\pi/2}^{\pi/2} [\mathcal{A}(k) + \mathcal{A}(-k + \pi)] dk \quad (C9)$$

and then be simplified as

$$P = \int_{-\pi/2}^{\pi/2} -i \nabla_k \log \det B(k) dk \quad (C10)$$

$$= -i \log \frac{\det B(\pi/2)}{\det B(-\pi/2)} \quad (C11)$$

The P is only meaningful mod 2π , as the ambiguity from the log gives $2\pi l$ where the l is an integer. So the P/π is of \mathbb{Z}_2 classification.

We note that at inversion center the eigenvalue (λ_i) of the inversion operator can be related to the determinant of the sewing matrix, by

$$\det B(k_{inv}) = \prod_i \lambda_i(k_{inv}) \quad (C12)$$

On the inversion invariant line, the P/π has quantized value, which corresponds to the π Berry phase, as shown in the Wilson loop diagrams in the main text. This explains why the cross of $\theta(k_y) = \pi$ happens at $k_y = \pi/2$, since $k_y = \pm\pi/2$ lines are the inversion invariant line.

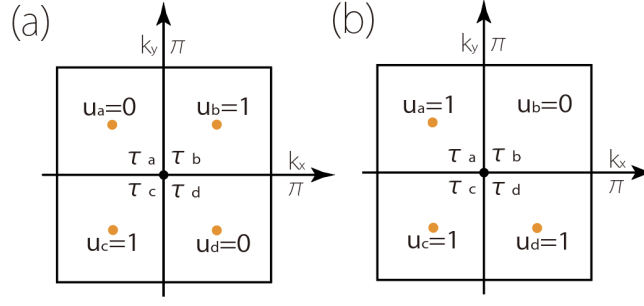


FIG. 9. Detect oddity of Chern number with the distribution of u_i . (a) corresponds to Chern number 0 or 2; (b) corresponds to Chern number 1. The Chern insulator here has momentum-non-centered chiral edge states.

In conclusion, we can formulate the u_i to relate the parity eigenvalue λ_i ,

$$(-1)^{u_a+u_b} = (-1)^{u_c+u_d} = (-1)^\nu = (-1)^{P_x/\pi} = \prod_j^2 \prod_i^N \lambda_i(\Gamma_j) \quad (\text{C13})$$

and similarly,

$$(-1)^{u_a+u_c} = (-1)^{u_b+u_d} = (-1)^{\nu'} = (-1)^{P_y/\pi} = \prod_j^2 \prod_i^N \lambda_i(\Gamma_j) \quad (\text{C14})$$

where Γ_j are inversion centers in the chosen half of the BZ. Different from the previous \mathbb{Z}_2 number, the Γ_j for the u_i do not coincide with the time-reversal invariant momenta, but are nonsymorphic, such that $\Gamma_j = (\pm\pi/2, \pm\pi/2)$.

Appendix D: Physical consequences of the momentum-non-centered inversion symmetry

There are other physical consequences associated with the momentum-non-centered inversion symmetry that are worth mention or further exploration. Here, we give two more specific directions.

1. Distribution of u_i as a mean to detect the oddity of Chern number

As another important symmetry in physics, time-reversal symmetry is a pure momentum inversion operation in spineless systems—a Hamiltonian with real coefficients. One intuition is that we can use the asymmetry distribution of the u_i relative to the origin point to indicate the breaking of time-reversal symmetry and to detect the Chern number. We define the $w_i = \frac{1}{2\pi} \int_{\tau_i} \mathcal{F}(\mathbf{k}) d^2\mathbf{k} - \frac{1}{\pi} \gamma(D+R)$. With time-reversal symmetry, the w_i should be anti-symmetric about the TRIM points, because the Berry curvature \mathcal{F} and the Berry phase γ are anti-symmetric under time-reversal symmetry. The w_i summing together equals zero. When the time reversal symmetry is broken, this analysis is invalid. In that case, we can use the u_i to detect the oddity of Chern number.

For example, in the H_{xy}^{2D} case, we realize Chern numbers from 0 to 2 by tuning the strength λ under the same symmetry. Notably, the oddity of the sum of the u_i reflects the oddity of the Chern number. For instance, in Fig. 9 (a) the $\sum_i u_i = 2$ which may correspond to the Chern number 0 or 2. In Fig. 9 (b), $\sum_i u_i = 3$ which may correspond to the Chern number 1 or 3. So we can distinguish the oddity of Chern number by the sum of u_i or equivalently the parity eigenvalues at the inversion center. As a result of nontrivial Chern numbers, Chern insulators with non-centered chiral edge states are guaranteed. See Fig. (c).

2. Nonsymorphic space-time inversion PT

Another interesting direction to be pursued for further research is the momentum-non-centered space-time inversion symmetry

$$\mathcal{PT} = U \mathcal{L}_{G_x/2} \mathcal{L}_{G_y/2} \mathcal{K} \quad (\text{D1})$$

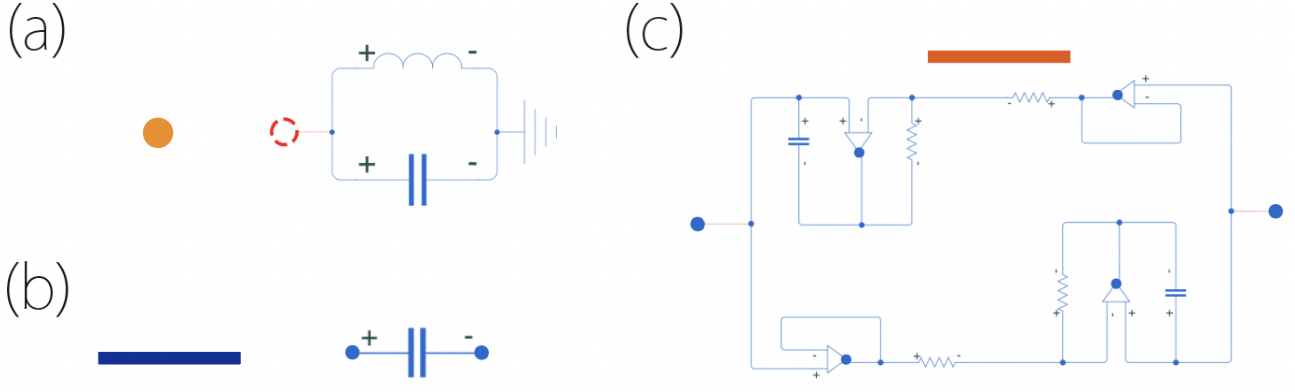


FIG. 10. Circuits modules that correspond to the lattice TB model in the Fig.3 (a) and Fig.2 (a). (a) The four sites in a unite cell corresponds to grounded L-C circuits; (b) the positive hopping amplitudes correspond to capacitors C ; (b) the negative hopping amplitudes corresponds to a circuit module with effective minus capacity $-C$;

or

$$\mathcal{PT} = U\mathcal{L}_{Gx/2}\mathcal{K}. \quad (\text{D2})$$

The Hamiltonian that obeys the first symmetry behaves as

$$\mathcal{PT}H(\mathcal{PT})^\dagger = H \quad (\text{D3})$$

$$UH^*(k_x + \pi, k_y + \pi)U^\dagger = H(k_x, k_y). \quad (\text{D4})$$

Appendix E: Experimental design of the artificial topological circuits

We now demonstrate our circuits setup that corresponds to the TB models and give first-principles simulation results for the $(\pm\pi/2, \pm\pi/2)$ case as an example.

Our circuits are made of capacitors and inductors and can eventually map the eigenvalue with frequency ω . We first recall that the effective resistances for a capacitor (C) and an inductor (L) are $j\omega C$ and $\frac{1}{j\omega L}$. Every components of the lattice TB models defined in the Fig. 3 (a) or Fig. 2 (a) have their circuits correspondences. See Fig. 10. The π -flux can be implemented by an effective minus capacitance $-C$ which can be realized by a circuit module in Fig. 10 (c)[10].

Circuits' Laplacian corresponding to the model can be obtained by Kirchhoff's current (or voltage) law[8]. Considering the current on every sites I_i , we have

$$I_i = \sum_{k=1}^4 [j\omega C_{ki}(V_k - V_i)] + \left(j\omega C_{Gi} + \frac{1}{j\omega L_{Gi}} \right) (V_G - V_i) = 0 \quad (\text{E1})$$

where $i = 1, 2, 3, 4$ represents the four sites in a unite cell. The C_{ki} or C_{Gi} represents the capacitors that are between the node k or the ground (G) and the node i . In practice, we have $V_G = 0$ V. All L_{Gi} between the ground (G) and sites i have inductance of L_0 , i.e., $L_{Gi} = L_0$. Solving the linear equation group from Eq. (E1) with $i = 1, 2, 3, 4$ gives us an Schrodinger liked equation

$$H_c\psi_c = E_c\psi_c \quad (\text{E2})$$

with the eigenvalue $E_c = \frac{1}{2\pi\omega^2 L_0}$ and the eigenstate $\psi_c = (V_1, V_2, V_3, V_4)^T$. The H_c is an effective 4-by-4 matrix derived from the circuit system. Considering the periodicity in the circuits' lattice, we perform Fourier transformation to H_c and obtained $H_c(\mathbf{k})$ in the momentum space. Here we provide correspondence between the H_c and the general Hamiltonian for the TB model H_0 in the Eq. (A1). In topological circuit, the energy is mapped to frequency of circuit, which are positive real numbers. So we first shift the original H_0 by μ such that all eigenvalues are positive. In circuits,

this can be controlled by the onsite capacitors C_{Gi} . As defined in Fig. 10, the hopping amplitudes correspond to the capacitors with factor differences

$$C_i = -C_0 h \quad (\text{E3})$$

$h = tm_i, lm_i$ $i = 1, 2$ are the hopping amplitudes, and C_0 is the unite for the capacitors. The capacities for the onsite capacitors, C_{Gi} , can be solved relative to the shift in chemical potential μ , as

$$C_{Gi} = \mu - \sum_i C_i \quad (\text{E4})$$

As a consequence, we map the H_c to the H_0 by

$$H_c = C_0(-H_0 + \mu) \quad (\text{E5})$$

and the ω to the E_0 obtained from H_0 by

$$\omega = \frac{1}{2\pi} \sqrt{C_0 L_0 (-E_0 + \mu)} \quad (\text{E6})$$

We do simulations to the $H^{(\pm\pi/2, \pm\pi/2)}$ as an example to show the validity of our circuits setup. We simulate the edge spectra for the circuits which demonstrate the non-centered inversion symmetry for slab geometries with thickness of 21 unite-cells in one direction and periodicity in the other. The simulation results are shown in Fig. 6 in the main text. Notably, the simulation results are in good agreement with theoretical predictions. The Fermi energy is shifted in accordance to the Eq. (E6) to 5.033 MHz.

In our simulations, we set $C_0 = 100$ pF, $L_0 = 1\mu\text{H}$, $\mu = 10\text{eV}$. Other circuits parameters can be obtained with this parameters and the parameters for TB model: $t_1 = 1.5$, $t_2 = 5.5$, $tm_1 = 1.5$, $tm_2 = 5.5$, $lm_1 = 1.0$, $lm_2 = -1.0$, $l_1 = 1.0$, $l_2 = 1.0$, and $\lambda = 0$ in the unite of eV.
